Slope selection-driven Ostwald ripening in ZnO thin film growth

A. González-González,[1,*] C. Polop,[2] and E. Vasco[1]

[1]*Instituto de Ciencia de Materiales de Madrid, Consejo Superior de Investigaciones Científicas (CSIC), 28049 Madrid, Spain*

[2]*Departamento de Física de la Materia Condensada, Universidad Autónoma de Madrid, 28049 Madrid, Spain*

(Received 28 March 2012; revised manuscript received 1 June 2012; published 23 July 2012)

The morphology evolution of polycrystalline ZnO films grown by pulsed laser deposition was investigated by atomic force microscopy and compared with morphologies simulated in 2 + 1 dimensions from a mesoscopic continuum model of selection of surface slopes. The distinctive feature of such an evolution is that the competition between grains gives rise to a singular grain coarsening mechanism, which although it matches the fingerprints of the Ostwald ripening, it remains operative under atypical growth conditions (temperatures as low as $0.28T_{\text{melting}}$ and grains with sizes ranged between 20–500 nm) and is driven by the faceting of the grain faces. The resulting pyramidal single-crystalline grains from such a coarsening mechanism have been correlated with the enhanced ultraviolet lasing activity at room temperature of nanostructured ZnO.

DOI: 10.1103/PhysRevB.86.045434 PACS number(s): 68.43.Jk, 68.37.Ps, 81.16.Rf, 68.55.J−

I. INTRODUCTION

In the context of the physics of crystal growth, Ostwald ripening (OR) is a well-known mechanism of coarsening[1] of surface species and/or grains (entities hereafter), in which the larger entities grow, drawing atoms from the smaller ones that shrink by atomic dissociation in order to reduce the surface energy of the system.[2–6] This mechanism, which can be understood[7] as a kind of hierarchical cannibalism between isolated entities, requires: (i) that the entities exchanging adatoms are close together (with entity spacing $\ll$ diffusion length) so as the capture rate of the larger entity influences the rate of decay in size of the smaller one via local gradients of the adatom density;[2–6] (ii) moderate growth temperatures (typically $\geqslant 0.5T_{\text{melting}}$ for oxides and nitrides[5,8]) and low adatom densities (i.e. high-mobility growth conditions) in order to promote the efficient breaking up of the smaller entities, which takes place only for dissociation rates higher than the growth rates induced by the diffusive noise;[9] (iii) since OR is a relatively slow mechanism (that involves series of dissociations[10]), it is effective for small entities with sizes of a few tens of nanometers.[3,6,9] On the contrary, the coarsening between larger entities happens mainly through peer-to-peer coalescence processes and grain growth that involves phenomena of formation and grain boundary migration, massive rearrangement of atoms (e.g. during grain rotation), and generation of strains and inner defects with the consequent formation of noncompact entities (typically; these exhibit percolated morphologies).[11,12] Unlike the standard coalescence and grain growth, OR produces typically compact single-crystal entities with pseudo-equilibrium equiaxed shapes[13] since the border diffusion is faster than the dissociation, which means that the captured adatoms can diffuse along the entity perimeter and be attached to the nearest kinks before a new capture takes place.

In this paper, we identify a late OR mechanism involving large grains (with sizes ranging between 20–500 nm) at deposition temperatures as low as $0.28T_{\text{melting}}$ in ZnO films. The origin and the main characteristics of such an atypical mechanism are elucidated by addressing the morphology evolution of the ZnO films (described in terms of the evolution of the size and shape of the grains, their surface slopes, and morphological environments from both average values and distribution functions) through a mesoscopic continuum model of slope selection.

II. EXPERIMENT

[0001]-textured ZnO films were pulsed laser deposited (PLD) on Fe-doped InP(100) substrates using a KrF excimer laser ($\lambda_{\text{KrF}} = 248$ nm, laser fluence $= 4$ J/cm^2, and pulse frequency $= 10$ Hz) focused on ZnO ceramic targets located at 6 cm from the substrate and rotated at 20 rpm. The deposit was carried out at a high vacuum chamber (with base pressure of $\approx 8 \times 10^{-7}$ mbar) in the presence of a highly pure (99.999%) molecular-oxygen flux (with dynamic pressure of 0.1 mbar) at a temperature of $T = 623$ K ($0.28\ T_{\text{melting}}$). The growth rate was $F = 0.08$ nm/s, and deposition times ranged from $0 \leqslant t \leqslant 2 \times 10^4$ s (i.e. film thicknesses of $d = 50$–1600 nm). Afterwards, the film morphologies were investigated *ex situ* by atomic force microscopy (AFM),[14] operating in contact mode using ultrasharp silicon tips with a nominal radius of 2 nm and aspect ratios as high as 10 to achieve high-resolution images. The tip miscut was estimated to be within the range of 55–60° (that corresponds to a cutoff slope of $m_{\text{tip}} \geqslant 0.66$) on calibration samples. The tip effects on measurements by AFM on flatter morphological features are considered to be negligible, whereas the slopes detected beyond the cutoff value are ascribed to tip-induced artifacts.

III. RESULTS

Figure 1 outlines the morphology evolution of the ZnO films. We observe that, for early growth stages [$t < 2 \times 10^3$ s, Fig. 1(a)] the morphology is dominated by a high density of small Gaussian-like shaped grains that often impinge each other, termed mounds hereafter. For intermediate stages [2×10^3 s $< t < 1 \times 10^4$ s, Figs. 1(b)–1(c)], two sets of grains are distinguishable by their shapes and sizes: large grains with partially faceted flanks (i.e. formed by vicinal surfaces with constant slopes) and a sixfold in-plane symmetry (denominated pyramids hereafter), which are immersed within the background of mounds whose sizes decrease slightly. The density of mounds overcomes a fast decrease as the pyramids

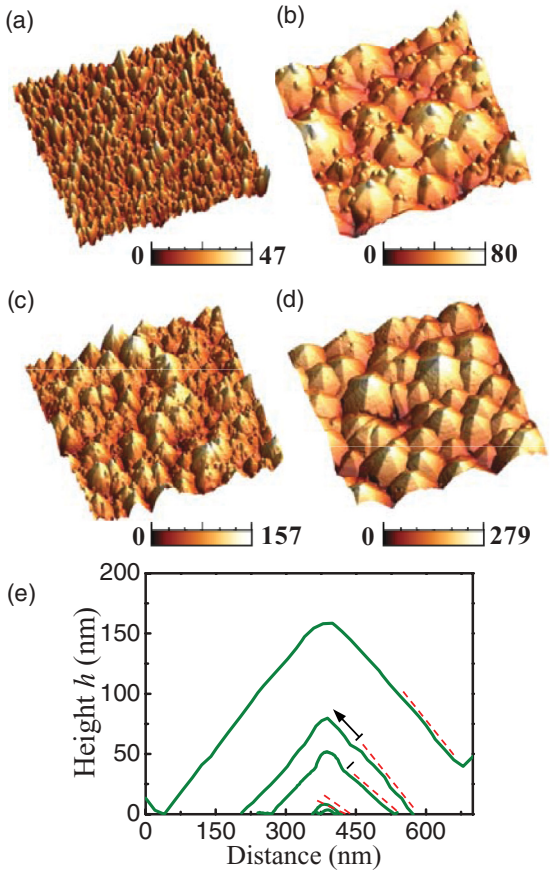

FIG. 1. (Color online) AFM images of ZnO films for different deposition times: (a) $t = 1.5 \times 10^3$ s, (b) 3×10^3 s, (c) 8×10^3 s, and (d) 1.8×10^4 s. The corresponding height scales (in nm) are included as color bars. Scanned area was 1×1 μm^2 in (a) and (b) and 3×3 μm^2 in (c) and (d). (e) Cross-section profiles taken over representative grains for each growth regime. Arrow indicates the direction of faceting propagation, whereas dashed lines (parallel to the grain flanks) assist in realizing the slope evolution.

coarsen, which indicates that mounds are incorporated into the pyramid bulks. For late growth stages [1×10^4 s $< t$, Fig. 1(d)], the surface is free of mounds, and it is fully covered by submicrometric pyramids with well-developed faceted faces, which impinge each other forming a compact arrangement of grains. Figure 1(e) highlights the profiles taken over representative surface features for increasing t, showing how the grain faceting starts at the bottom regions and propagates uphill to give rise to a full transformation towards pyramidal structures for late stages. The sixfold in-plane symmetry of pyramids results straightforwardly from the ZnO[0001]-texture of the films with the c axis of the *hcp* cell along the out-of-the-film plane direction.[15,16] Similar morphologies to those presented here have been obtained in ZnO films grown by other vapor deposition techniques, such as thermal evaporation, sputtering, and chemical etching.[17–19]

Figure 2 depicts the time evolution of several statistical parameters representative of the thin film morphology, namely: mound and pyramid densities, ρ^m and ρ^p, respectively, computed by direct counting using flooding procedures once classified the grains according their shapes [Fig. 2(a)]; surface slope m of the grains (without discerning between grain types)

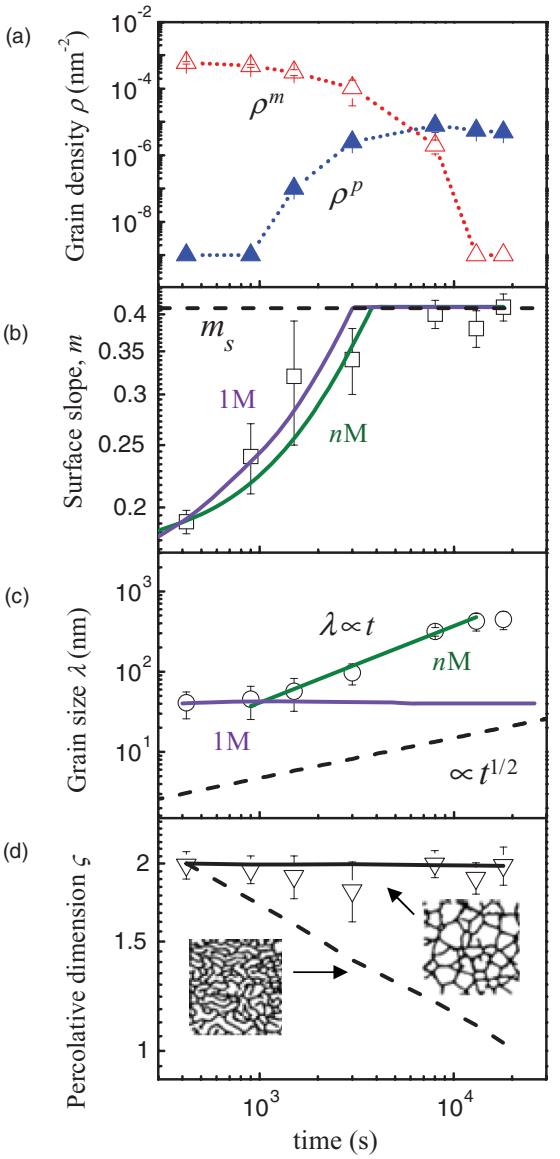

FIG. 2. (Color online) Evolution of statistical parameters representative of the film morphology, namely: (a) density of mounds ρ^m (△) and pyramids ρ^p (▲), (b) surface slopes m (□) with m_s denoting the selected one, (c) grain-size λ (○), and (d) fractal dimension ζ (▽). The curves correspond to: [solid ones] fitted and/or simulated results using single- (1M) or many-mound (nM) conditions; [dashed] expected and/or simulated behaviors for limit cases and/or saturation; and [dotted] lines connecting data points to guide to the eye. Insets in (d) show the percolated and compact-like morphologies (on the left and right, respectively) that result from solid-on-solid simulations concerning peer-to-peer coalescence and hierarchical atomic exchange with edge diffusion similar to OR, respectively.

estimated by means of a polynomial-based image processing procedure described elsewhere [Fig. 2(b)];[20,21] in-plane grain size λ (just grain size hereafter) estimated from the contour maps in the AFM images [Fig. 2(c)];[20] and fractal dimension ζ of the grain perimeter [Fig. 2(d)].[22] Figure 2(a) reveals that the increase in ρ^p takes place simultaneously with the decrease in ρ^m, which points out to the transformation of mounds into pyramids at a ratio—estimated from the corresponding steady densities—of 10^2 mounds per each formed pyramid.

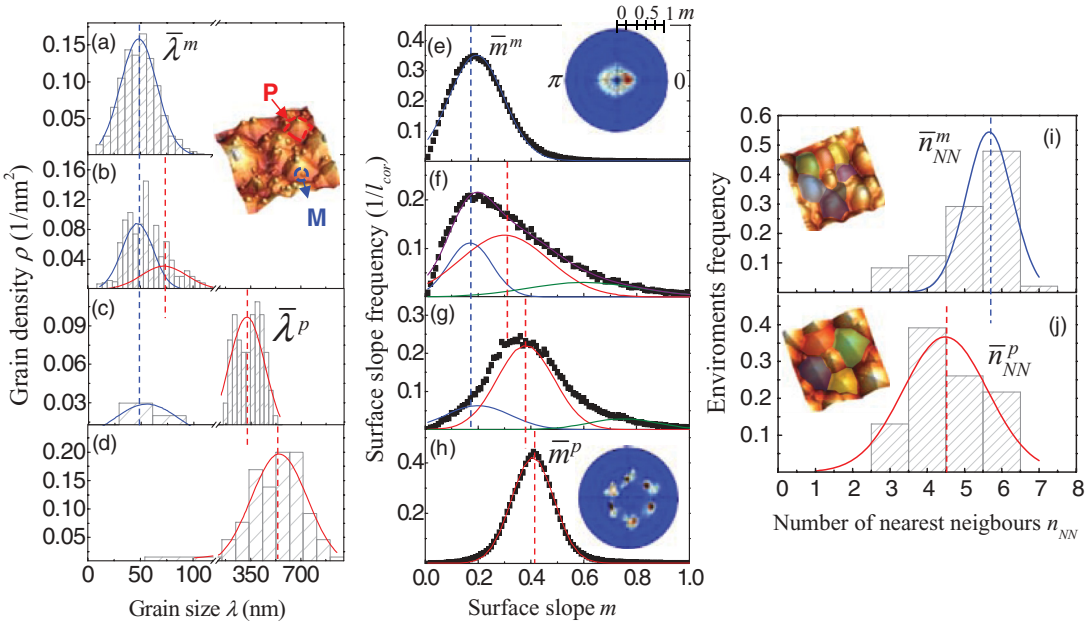

FIG. 3. (Color online) Evolution of the distribution functions $N(\ldots)$ of morphological statistical parameters, namely: (a)–(d) grain-size distributions $N(\lambda)$, (e)–(h) surface slope distributions $N(m)$,and (i)–(j) environment distributions in terms of numbers of nearest neighboring grains $N(n_{NN})$. The corresponding deposition times are: (a), (e), and (i) $t = 420$ s; (b) and (f) 1.5×10^3 s; (c) and (g) 8×10^3 s; and (d), (h), and (j) 1.8×10^4 s. Insets provide complementary information: (a) and (b) classification by size of the grains, (e) and (h) surface-orientation maps $N(m,\phi)$, where ϕ denotes the azimuthal coordinate providing in-plane information, and (i) and (j) representative morphological environments of the population of mounds and pyramids. We believe that high-slope green-curve components in (f) and (g), whose means are higher than the AFM-tip cutoff ($m_{\text{tip}} \approx 0.66$–$0.7$), correspond to tip-induced artifacts related to the abrupt changes of the slope on the grain flanks with the uphill faceting. Note this component disappears in (h) once the faceting has propagated to the whole flanks.

Figures 2(b) and 2(c) display the dynamics of faceting (the average slope increases up to reach a saturation value of $m_s = 0.41$) and coarsening ($\lambda \propto t^{1.0\pm0.1}$) of grains resulting from such a transformation. The selected slope $m_s = 0.41$, which corresponds to ZnO$\{10\bar{1}3\}$ facets, is lower than $m_s \approx 1.8$ (ascribed to ZnO$\{10\bar{1}\bar{1}\}$ facets) obtained under nearer-of-equilibrium conditions (i.e. at higher growth temperatures[17]). Additionally, this value is lower than the slope threshold corresponding to the estimated tip miscut, $m_{\text{tip}} \geqslant 0.66$, which is why tip effects are considered to be negligible in the determination of the slopes for the surface entities analyzed here. These arguments allow us to affirm that the faceting reported here corresponds to a kinetic process that results from the competition between surface currents rather than a thermodynamic faceting toward facets with lower surface energies.[23] The fact that the compact grain shapes are preserved during the growth [note that $\zeta = 1.9 \pm 0.1$ remains constant in Fig. 2(d)] for deposition temperatures as low as $0.28T_{\text{melting}}$ indicates that the transformation of mounds into pyramids takes place preferentially through atomic exchange by surface currents (i.e. it is an OR-type process), and thus the phenomena of coalescence and/or grain boundary migration play a minor role in both the coarsening and faceting of the pyramid-shaped grains. This statement is based on the fact that the phenomena of coalescence and grain boundary migrations involve only the boundary sections between neighboring grains, such that by randomly removing these sections, percolated grains are obtained whose fractal dimensions decrease as the grains coarsen, as plotted by the dashed curve in Fig. 2(d). Details on the fitted curves to the experimental data and those simulated for limit cases (solid and dashed curves, respectively) in Figs. 2(b)–2(c) are provided below.

In order to provide further information, Fig. 3 plots the time evolution of the normalized distribution functions $N(\ldots)$ of some statistical parameters: the distribution of grain sizes normalized by the AFM-scanned area [Figs. 3(a)–3(d)]; the distribution of surface slopes normalized per the number of uncorrelated areas in which can be subdivided the AFM image once interpolated [Figs. 3(e)–3(h)];[24] and the distribution of morphological environments in terms of the number of nearest neighboring grains n_{NN} [Figs. 3(i)–3(j)]. The corresponding insets provide insight on the classification by size of the grains, giving rise to the multimodal λ distribution [Figs. 3(a)–3(b)]; the evolution of the azimuthal ϕ dependence of the distribution of surface slopes $N(m,\phi)$ (also termed surface orientation map) [Figs. 3(e) and 3(h)];[21] and the representative morphological environments of the populations of mounds and pyramids in which the nearest neighbors of the central grains have been distinctively colored [Figs. 3(i) and 3(j)]. As a consequence of the transformation of the mounds into pyramids, a larger grain-size contribution [which is ascribed to the population of pyramid-shaped grains, red curve in Fig. 3(b)] emerges from unimodal distribution displayed in Fig. 3(a) (blue curve) that corresponds to the mound population. Further atomic exchange results in a shift of the λ distribution of the pyramids toward larger sizes (i.e. the pyramids coarsen) from a decay in the mound population, which disappears for late stages [see trend in Figs. 3(a)–3(d)]. Once the resulting pyramids become larger than 100 nm, both the faceting of their flanks toward

ZnO{10$\bar{1}$3} planes (realized as a shift of the m distribution toward $m \rightarrow m_S \approx 0.41$) and the grain texturing (giving rise to sixfold in-plane symmetry) take place as shown in the series of Figs. 3(e)–3(h). Additionally, the data in Figs. 3(i)–3(j) indicate that the thus-formed pyramids are arrayed in less compact arrangements than the departing mounds since the average number of nearest neighboring grains decreases from $\bar{n}^m_{NN} = 5.8$ [mounds, Fig. 3(i)] down to $\bar{n}^p_{NN} = 4.5$ [pyramids, Fig. 3(j)]. A fact to stress of these results is that the grain size and morphological environment distributions of the pyramid population are broader than those of the mound population, whereas its surface slope distribution is narrower than the corresponding one. This suggests that, whereas the differences of grain size and/or the morphological environments between mounds rule the intermound and mound-pyramid atomic exchanges (similar to the typical OR) by selecting which grain survives and which one perishes such that only small size and environment deviations are possible, these differences do not appear to be important for the pyramid faceting. Instead, our results point out that the difference of the surface slopes between neighboring pyramids would play here a key role on the atomic exchange between pyramids.

IV. DISCUSSION

A. Model

In the first part of the discussion, we analyze the striking behavior of the slope saturation (faceting) during the formation of pyramid-shaped grains in terms of the interactions between the small grains with mound shapes. With this aim, we employ a continuum mesoscopic model of slope selection. In this model, the morphology transformation of mounds into pyramids is attributed to asymmetries between the intra- and interlayer mass transports caused by the existence of step-edge barriers.[23,25] Such an asymmetry is described in terms of the balance between the local currents, namely: uphill and downhill surface currents (denoted as J^{up} and J^{down}, respectively) to what the following mechanisms contribute: J^{up} leads the fraction of adatoms reflected by the step-edge barriers and those deposited preferentially on the upper terraces (by steering) into the ascending steps; whereas J^{down} is given by the fraction crossing the step-edge barriers (e.g. via atomic exchange) plus those deposited downwards (by funneling).[25] In this context, the selected slope m_s corresponds to a metastable state in which the grain shapes (in particular their aspect ratios) are preserved, which means that $\partial_t m|_{m_s} \propto J^{\text{up}}(m_s) - J^{\text{down}}(m_s) \approx 0$. For small perturbations around m_s, the balance $J^{\text{up}}(m_s) = J^{\text{down}}(m_s)$ shifts to $J^{\text{up}} < J^{\text{down}}$ for $m = m_s + |\delta m|$ and $J^{\text{up}} > J^{\text{down}}$ for $m = m_s - |\delta m|$ in order to stabilize the morphological slope toward its selected value m_s.[23,25–30]

A generalized equation at mesoscopic scale (where a continuum approach to the film surface $h(\vec{r},t)$ is pertinent, with $\vec{r}$ being a position vector within the film plane) that describes the kinetics of the phenomenon of slope selection was proposed by Johnson *et al.*:[26]

$$\frac{\partial h(\vec{r},t)}{\partial t} = -\alpha\nabla\left(\frac{\nabla h(\vec{r},t)}{m_s^2 + [\nabla h(\vec{r},t)]^2}\right) + \Phi(\vec{r},t) + \eta(\vec{r},t), \tag{1}$$

where $\alpha = aFl_d^2(1 + e^{-E_a/k_BT})$ is a kinetic constant that takes into account the contribution of the atoms landing within a strip l_d of the surface (with lattice parameter a) around the steps to the surface currents via diffusion (whose activation energy E_a depends on the local environment); $\Phi(\vec{r},t)$ comprises the relaxation mechanisms identified here with the surface curvature-driven Mullins–Herring diffusion $\Phi(\vec{r},t) = -\kappa\nabla^4 h$ with $\kappa = D_s\rho_e^1(\bar{\lambda})\varepsilon_s\Omega/k_BT$ [where $D_s \propto e^{-E_a/k_BT}$, $\rho_e^1(\bar{\lambda})$, and ε_s correspond to the surface diffusion coefficient, the equilibrium adatom density in a surface with an average grain size of $\bar{\lambda}$, and the surface energy, respectively]; and $\eta(\vec{r},t)$ encloses the uncorrelated Gaussian noise generated by stochastic perturbations of both the growth rate F and temperature T.[25,26,31] k_BT/Ω denotes the thermal energy per atomic volume Ω of the system during the process.

The first term in Eq. (1), which can be rewritten as $\alpha[-f_1(\nabla h) + f_2(\nabla h)]\nabla^2 h$ with $f_1(\nabla h) = [m_s^2 + (\nabla h)^2]^{-1}$ and $f_2(\nabla h) = \nabla h \cdot \partial_{\nabla h} f_1(\nabla h)$, defines the morphology evolution towards grain shapes with constant slopes (conical or pyramidal depending on the system in-plane symmetry) through the competition between two complementary mechanisms: (i) a Kuramoto–Sivashinsky-type destabilization of the surface $-\alpha \cdot f_1(\nabla h) \cdot \nabla^2 h$ (Ref. 32) and (ii) a Edwards–Wilkison-type surface relaxation $\alpha \cdot f_2(\nabla h) \cdot \nabla^2 h$.[33] The functions $f_1(\nabla h)$ and $f_2(\nabla h)$ describe the slope modulation of the faceting kinetics as follows. For very small slopes (with $\nabla h \rightarrow 0$), the destabilization mechanism prevails $[-f_1(\nabla h) + f_2(\nabla h)] \approx -(\nabla h)^2$, generating intense uphill currents that produce an increase in the slope at a decreasing rate $\propto \alpha/(\nabla h)^2$. The intensity of the uphill current decreases down to vanish for a facet with the selected slope $|\nabla h| = m_s$, in which the equilibrium condition between both mechanisms $[-f_1(\nabla h) + f_2(\nabla h)] = 0$ is reached, giving rise to a steady grain shape $h'(\vec{r})$ with $\partial_t[h \rightarrow h'] \rightarrow 0$. Conversely, for slopes $|\nabla h| \gg m_s$, the capacity of relaxation of the surface prevails $[-f_1(\nabla h) + f_2(\nabla h)] \approx (\nabla h)^{-2}$ generating a weak downhill current that leads to a slow recovery of the facet with selected slope.

B. Interpretation of the results in the light of the model

Figure 4 displays the morphology evolution of a single mound controlled by the slope-selection mechanism described in (1). The initial mound shape was taken from the experimental results and fitted to a Gaussian three-dimensional (3D) function $h(r,0) = h_0^m e^{-(r/2\lambda_0^m)^2}$ [pictured in Fig. 4(a) whose profile is plotted in Fig. 4(d), blue curve] with $\lambda_0^m = 40$ nm [mound size as shown in Fig. 2(c)] and $h_0^m = 5$ nm [mound height, from combining Figs. 2(b) and 2(c)]. The 2D + 1 simulation shown in Figs. 4(a)–4(c) is performed for a coefficient ratio $\alpha/\kappa = 0.07$, which is estimated by fitting the simulated faceting kinetics to the average slope evolution plotted in Fig. 2(b), and a selected slope of $m_s = 0.41$ (the experimental saturation slope).[34] Both thus obtained α/κ and m_s describe the faceting kinetics well in vicinal surfaces with moderate step-edge barriers as revealed from the good agreement with the corresponding parameters computed by kinetic Monte Carlo simulations.[26] The final mound profile is included in Fig. 4(d) as a red curve for comparison purposes. As the growth happens, two key features of the morphology

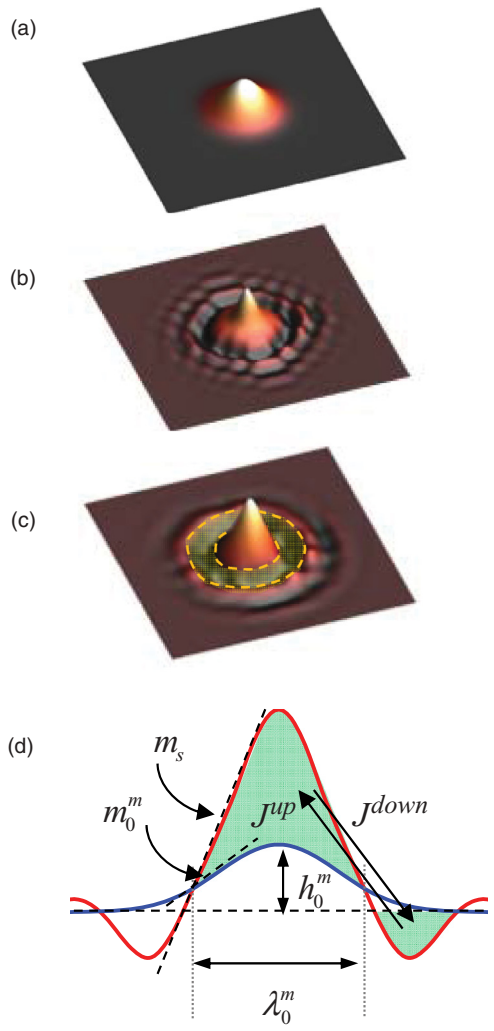

FIG. 4. (Color online) (a)–(c) Simulated morphology evolution of a single mound-shaped structure ruled by the slope-selection mechanism described in (1). As the growth proceeds, a surrounding depletion zone is observed, as outlined in (c). (d) Cross-section profiles at different growth stages: (blue curve) initial stage in which the morphological features of the mound-shaped structure—namely: size λ_0^m, height h_0^m, and the highest slope m_0^m—are depicted; and (red curve) final stage, which corresponds to the profile of a conical/pyramidal-shaped structure with constant slope m_s along the flanks. Shaded regions sketch the conservative mass transport through the balance between $J^{\rm up}$ and $J^{\rm down}$ currents.

evolution are identified: (i) the formation of a trench-like depletion zone around the mound perimeter and (ii) the development of sharp apexes at intermediate times. This latter feature arises as a consequence of the Gaussian 3D function chosen for modeling the mound shapes having a maximum value of curvature $\propto -\nabla^2 h(\vec{r},t)$ on mound top, such as the strength of the Kuramoto–Sivashinsky-type mechanism is enhanced within theses regions, speeding up the faceting. Once the slopes within the apex regions reach the selected slope, the apex shapes remain constant. Note that these sharp apexes should not be related with those rounded ones on the pyramidal trunks in Fig. 1(b), whose origin is the uphill propagation of the faceting. An inspection of the series of simulated images [Figs. 4(a)–4(c) and no shown intermediate images] confirms the fact pointed out in Fig. 1(e) that the faceting kinetics start at the grain bottom and propagate up via uphill currents that drain material from the depletion zone. For longer growth times [Fig. 4(c)], the selected slope has propagated to the whole flank, giving rise to the full transformation of mounds into conical structures, as revealed by red profile in Fig. 4(d). The time dependence of both the slope averaged on the grain flank and the grain size computed from the simulation for a single mound are included in Figs. 2(b) and 2(c) (solid curves labeled 1M) to be compared with the experimental data. From these comparisons, we can conclude that the single-mound slope-selection model reproduces well the experimental morphology evolution of the grains [good agreement in Fig. 2(b)] with regard to the faceting kinetics giving rise to the shape transformations of isolated mounds into conical/pyramidal grains; however, this does not explain the grain coarsening behavior observed experimentally [see Fig. 2(c)].

Figure 5(a) discloses some relevant aspects of the simulated morphology evolution for a single mound that play key roles when several grains are considered. In particular, Fig. 5(a) provides details of the profiles of the depleted zones generated around grains with different sizes λ (compare curves A and B), different selected slopes m_s (curves A and C), and kinetic coefficient ratios κ/α differing in several orders of magnitude (curves A and D). From the profiles, two characteristic parameters (which are linked closely to the depletion kinetics) can be defined: the capture length ξ that corresponds to the distance beyond the grain perimeter where the depletion is highest (i.e. where the profile has a minimum), and the capture rate $1/\tau$ (with τ being the characteristic draining time of the depletion phenomenon) such that the depth of the profile minimum (at ξ) for a given runtime t is $\propto t/\tau$. The dependence of these parameters on λ, m_s, and κ/α are log-log plotted in Figs. 5(b)–5(c). Whereas ξ depends only on λ through the power-law dependence $\xi \propto \lambda^\beta$ with $\beta = 1.0 \pm 0.2$ for wide ranges of $0.1 \leqslant m_s \leqslant 1.0$ and $0.01 \leqslant \alpha/\kappa \leqslant 1000$ [see the dataset collapse in Fig. 5(b)]; τ is roughly independent on both λ and α/κ, exhibiting a power-law dependence only on m_s [Fig. 5(c)]: $\tau \propto (m_s - m)^\varphi$ with $\varphi = 1/3 \pm 0.01$. In brief, larger (steeper) pyramidal-shaped grains give rise to wider (deeper) depletion zones. From these dependencies, we can throw light on the nature of the depletion phenomenon as well as on the physical meanings of both ξ and τ. The fact that τ does not depend on ξ (note that both depend on independent variables) points to a depletion phenomenon driven by drift, i.e. by biased mass transport rather than by diffusion-limited aggregation for which $\tau \propto \xi^2$, as predicted. Thus, the drain of the captured atoms would take place through biased random paths that become more ballistic and less random-walk as the capturing grain is larger. It would addresses the capability of the larger grains to capture far atoms (at $\xi \propto \lambda$) at the same rate (as $\partial_\lambda \tau \approx 0$) than the smaller grains capture near atoms. This conclusion explains also the independence of both ξ and τ on κ/α as a consequence of the grain sizes are larger than the space scale ($\approx\sqrt{\kappa/\alpha}$) in which the surface diffusion plays a preponderant role, which means that the diffusion becomes negligible at intergrain scale. The value range of κ/α used for the simulations in Fig. 5 was thus chosen on the basis of previous reports[35–38] from which a diffusion length

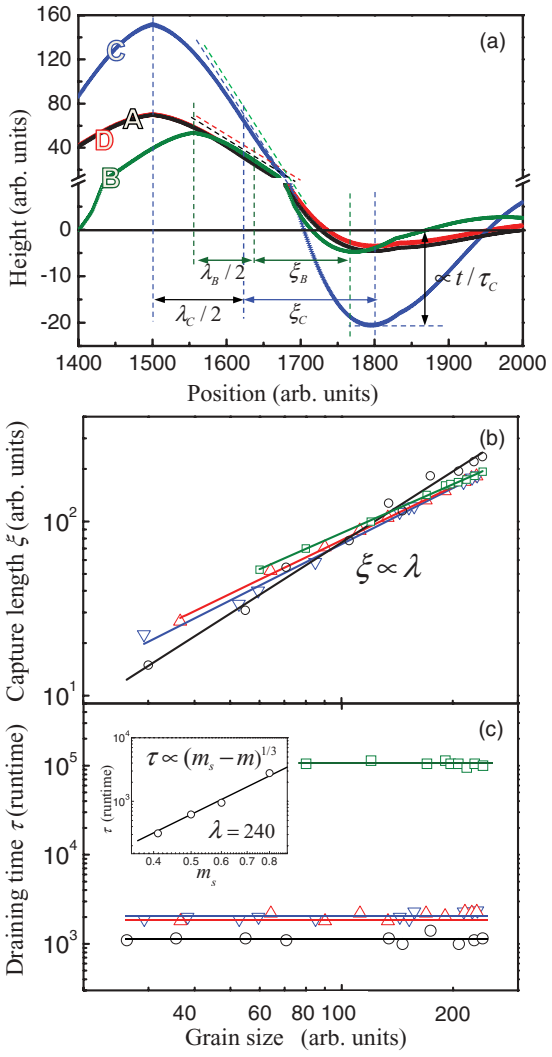

FIG. 5. (Color online) (a) Cross-section profiles of simulated mound-shaped structures after faceting by a slope-selection mechanism. Curve labels and subindexes indicate the sets of used parameters for simulations: $A \rightarrow \{\kappa/\alpha = 0.01,\ m_s = 0.41,\ \lambda = 400\}$, $B \rightarrow \{\kappa/\alpha = 0.01,\ m_s = 0.41,\ \lambda = 300\}$, $C \rightarrow \{\kappa/\alpha = 0.01,\ m_s = 1.0,\ \lambda = 400\}$, and $D \rightarrow \{\kappa/\alpha = 1000,\ m_s = 0.41,\ \lambda = 400\}$. Note that a break in the height axes has been inserted to assist in realizing the magnitudes: λ, structure size estimated from the full width at half maximum of the mound profiles; ξ, capture length defined as the distance beyond $\lambda/2$ where the profile has a minimum; and τ, draining time, such as the profile depth at the minimum position becomes $\propto 1/\tau$ (i.e. t/τ for a given runtime t). Here, λ dependence of ξ and τ are log-log plotted in (b) and (c), respectively. In both cases, the used symbols define the sets of parameters for simulations: $(\circ) \rightarrow \{\kappa/\alpha = 1.0, m_s = 0.3\}$, $(\square) \rightarrow \{\kappa/\alpha = 1.0, m_s = 1.0\}$, $(\Delta) \rightarrow \{\kappa/\alpha = 1000.0, m_s = 0.41\}$, and $(\nabla) \rightarrow \{\kappa/\alpha = 0.01, m_s = 0.41\}$. Solid lines in (b) and (c) represent the best fit of the simulated data to scaling dependences based on power-law functions. The inset in (c) shows the m_s dependence of τ for the larger structures.

of ≈100 nm could be estimated for ZnO films at 623 K, and it is in the same order of magnitude of that employed in growth simulations of metal surfaces.[26] Note that such a diffusion length is several times shorter than the sizes of the pyramidal-shaped grains.

Once the main characteristics of the slope-selection model computed for single mounds have been discussed, a simulation considering many mounds (which compete with each other at length scale ξ) has to be performed in order to address the grain coarsening behavior, as shown in Fig. 2(c). Figure 6 displays the simulations for three kinds of grain competitions:

(i) Figure 6(a): Competition in terms of the morphological environment between grains with similar sizes and similar surface slopes $m \ll m_s$ so as the grains with a number of nearest neighboring grains n_{NN} higher than the average number $\bar{n}_{NN}$ decays [shrinkage of the central mound with six neighbors, green curve in Fig. 6(d)], whereas those within rarefied environment coarsen [growth of a no shown mound with four neighbors, red curve in Fig. 6(d)].[6] The results in Figs. 3(a) and 3(j) showing the narrow grain-size distribution and the different morphological environments of the mound population, respectively, suggest that this type of competition acts as a selection mechanism of a few mounds (those that coarsen) to become pyramidal/conical grains. This suggestion is: (a) inspired on the decrease in the average number of neighbors per resulting pyramid, which cannot be explained through a model of isotropic/compact depletion; and (b) supported by the results in Figs. 3(a)–3(d) that reveal the breakup of the unimodal grain-size distribution into two populations (blue and red curves), whose average sizes exhibit dissimilar behaviors (remain slightly constant and increase, respectively) with the deposition time.

(ii) Figure 6(b): Competition between two grains with different sizes and similar surface slopes $m \ll m_s$. Once the average sizes of the two grain populations differ significantly, the competition becomes ruled by the grain sizes λ through the capture length ξ. As a consequence of the λ dependence of ξ [Fig. 5(b)], a lot of mounds are within the depletion zones of the pyramidal/conical grains, while only a few of these latter are affected partially by the capture of so-close mounds. Thus, the grain-size-based competition would be responsible for the decay in the density of mounds [as shown in Fig. 2(a)] and the coarsening of the pyramidal/conical grains [Fig. 2(c)].

On the basis of our results in Figs. 2(a) and 3(a)–3(d), we can assume that many small mounds dissociate slowly (which implies $\partial_t \rho^m \gg \partial_t \lambda^m$, i.e. the mound density drops faster than the mound shrinkage), proving the adatom flux for the quick growth of a few conical/pyramidal grains ($\partial_t \rho^p \ll \partial_t \lambda^p$). This assumption is supported by the fact that the ratio between the corresponding steady densities is $\rho^m_{t\rightarrow 0}/\rho^p_{t\rightarrow\infty} \sim 10^2$ [Fig. 2(a)], which means that a single pyramidal grain results from the dissociation of 10^2 mounds in average. For conservative systems (like that analyzed here where the re-evaporation of the adatoms generated from the mound dissociation is neglected), the mass-conservation condition $\partial_t \chi^p = -\partial_t \chi^m$ is satisfied in terms of the densities of adatoms $\chi^m = \frac{\pi}{4\Omega} h^m (\lambda^m)^2 \rho^m$ and $\chi^p = \frac{\sqrt{3}}{16\Omega} m_0^p (\lambda^p)^3 \rho^p$ that compose the mounds and the pyramidal grains, respectively. By rewriting the mass-conservation condition from the assumption described above, we get an expression to calculate the coarsening rate of the pyramidal grains:

$$\frac{\partial}{\partial t}\lambda^p \approx -\frac{4\pi}{3\sqrt{3}} \frac{h^m}{m_s \rho^p_{t\rightarrow\infty}} \left(\frac{\lambda^m}{\lambda^p}\right)^2 \frac{\partial}{\partial t}\rho^m. \qquad (2)$$

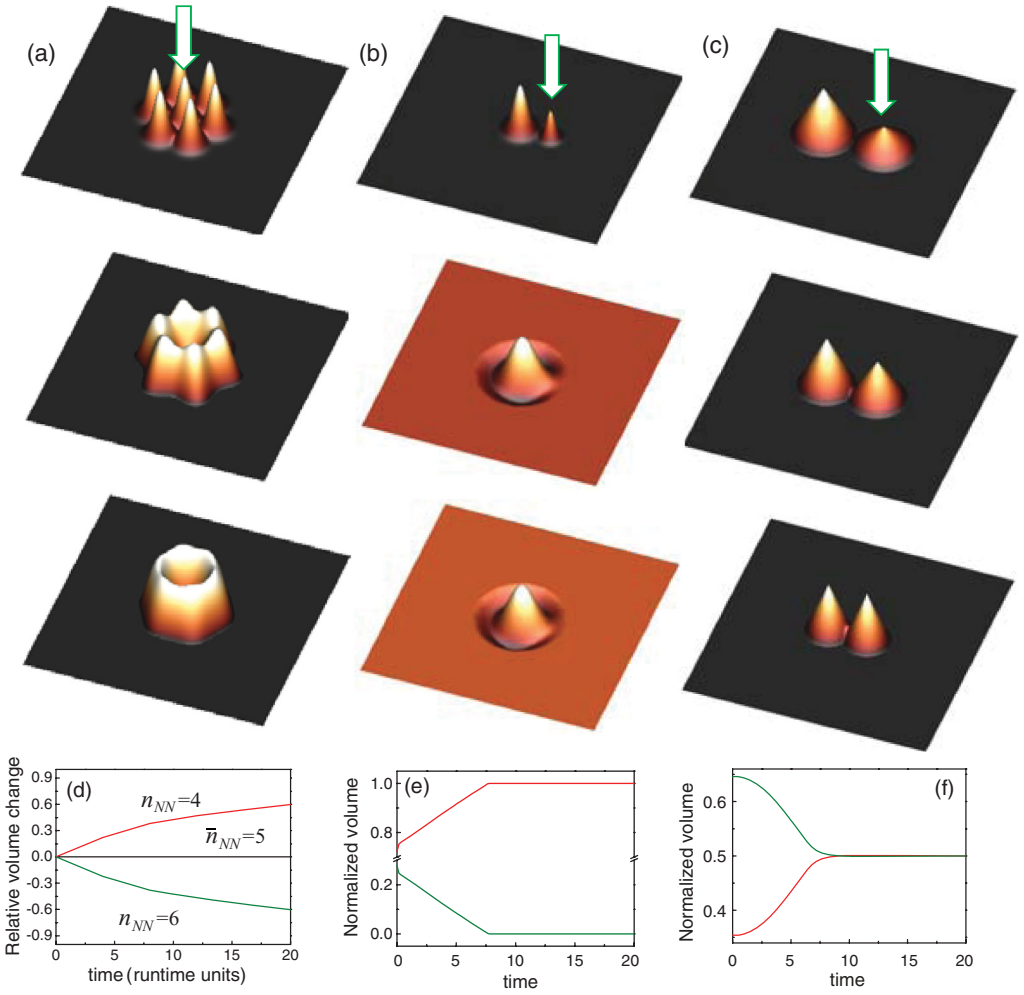

FIG. 6. (Color online) Simulated grain coarsening by competitive growth based on: (a) different morphological environments (same-sized grains with $m \ll m_s$ and $n_{NN} = 6$ for the central grain), (b) grain-size differences (dissimilar-sized grains with $m \ll m_s$), and (c) surface-slope differences (same grain size with m's $\approx m_s$ and $\leqslant m_s$ for the left- and right-hand grains, respectively). The arrows point to the involved grains with the highest relative volume variations. Graphs in (d)–(f) show the time dependence of the grain coarsening (expressed here in terms of volume changes) for the different kinds of competitive growths. Plot in (d) depicts the relative grain-volume variations (i.e. with respect to the initial grain volume) for grains that decay/grow within dense/rarefied environments with $n_{NN} = 6/n_{NN} = 4$ assuming $\bar{n}_{NN} \approx 5$ from Fig. 3(j); whereas those in (e) and (f) exhibit the variations normalized with regard to the considered total volumes $\sum_{\text{grain population}}$.

At this point, $\partial_t \rho^m$ is estimated from the scaling dependence in Fig. 5 that indicates that the mound population is depleted beyond the pyramidal-grain perimeter $\propto \lambda^p$ by a capture length $\xi \sim (\lambda^p)^\beta$ at a rate of $1/\tau \sim (m_s - m)^{-\varphi}$ such that $\partial_t \rho^m \propto -\rho^p_{t\to\infty}\rho^m_{t\to 0}\lambda^p \xi/\tau \sim (\lambda^p)^{1+\beta}$. This estimation leads to a power-law coarsening dependence:

$$\lambda^p \cong \Theta \cdot t^{1/(2-\beta)} \tag{3}$$

with $\Theta = \sqrt[2-\beta]{\rho^m_{t\to 0}/16\Omega(2-\beta)\sqrt{\kappa/27\alpha}}$. By substituting $\beta = 1.0 \pm 0.2$ in Eq. (3), we get $\lambda^p \sim t^{1.0\pm0.2}$, which is in good agreement with the experimental coarsening rate found in Fig. 2(c) that shows the pyramids growing as $\lambda^p \sim t^{1.0\pm0.1}$. Note this agreement proves the fact that the capture and drain within the depletion zones take place through biased mass transport, as discussed above, to address the independence on ξ of τ. Otherwise, by assuming a hypothetical scaling dependence $\tau \propto (\xi)^\psi \sim (\lambda^p)^{\psi\beta}$(where $\psi = 2$ for the case of random-walk diffusion), $\partial_t \rho^m \sim (\lambda^p)^{1+\beta(1-\psi)}$ and so $\lambda^p \sim t^{1/[2-\beta(1-\psi)]}$ that would be in accordance with the experimental results in Fig. 2(c) only for $\psi \approx 0.0 \pm 0.2$.

(iii) Figure 6(c): Competition between faceted grains with surface slopes close to m_s. Under these conditions, the small currents between neighboring grains are insufficient to alter both the grain density and/or the morphological environments, especially when the grains are large enough. This competition that operates between the pyramidal-shaped grains would stabilize the surface slopes toward their saturation value that corresponds with the selected slope [in agreement with Fig. 2(b)] and would preserve by mass-conservation the average size of the pyramid population [Fig. 2(c)]. Once the local grain slopes are stabilized, the surface of regular pyramidal structures becomes steady.

Figures 7(a)–7(c) display the morphology evolution of a many-mound surface controlled by the slope-selection mechanism described in Eq. (1). The initial morphology is

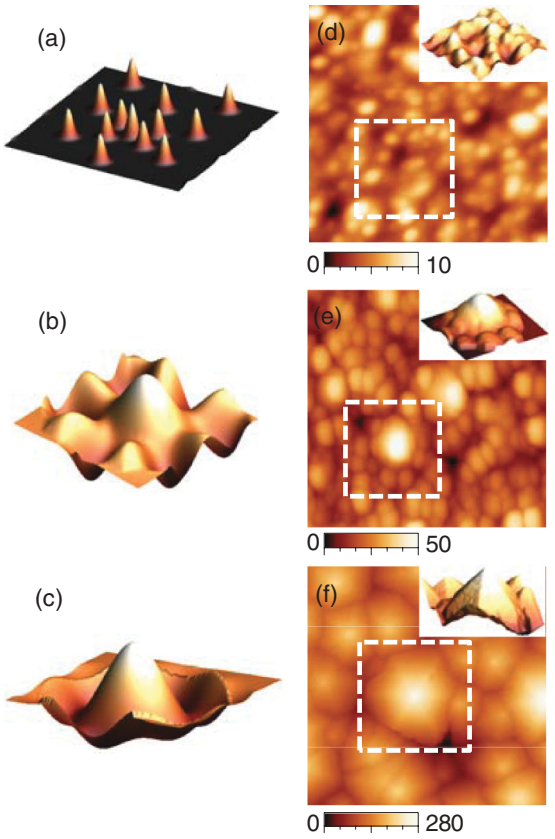

FIG. 7. (Color online) (a)–(c) Simulated morphology evolution of a many-mound surface ruled by the slope-selection mechanism described in (1) to be compared with the top-view AFM-images in (d)–(e). The direct comparison takes place with the outlined local environments, whose cross-section views are in the corresponding insets. Scanned area by AFM was 500 × 500 nm^2 in (d) and (e) and 2 × 2 μm^2 in (f). Height scales (bottom color bars) are in nm. Note that the sixfold in-plane symmetry of the resulting pyramids are a consequence of the ZnO[0001]-texture of the films, which is irrelevant for our study that deals with the intergrain competitive growth rather than intragrain recrystallization.

formed initially by an array of uniform-sized mounds, in which the different morphological environments are considered by locating the mounds at random positions. Periodic boundary conditions are assumed in order to avoid finite-sized artifacts. The series shown in Figs. 7(a)–7(c) correspond to successive growth stages generated by competitive growth illustrated in Fig. 6. The thus-simulated surfaces are directly compared with local environments observed in the corresponding AFM-imaged morphologies, as depicted in Figs. 7(d)–7(f) and the corresponding insets.[39] The qualitative agreement between the simulated morphologies and AFM-imaged ones is apparent, and so it supports the soundness of the investigated model.

The slope-selection mechanism reported here is classified as an OR-type process on account of the following fingerprints. The grain coarsening results from the atomic exchange via surface currents between isolates entities giving rise to compact grains with pseudo-equilibrium shapes; whereas (as predicted by the SZM model[40]) potential phenomena of bulk recrystallization involving grain-boundary migration are suppressed at the used deposition temperatures ($0.28T_{melting}$). Nevertheless this classification, the slope-selection mechanism corresponds to an atypical OR regarding both the driving force for the atomic exchange between the involved entities and the scenario in which this mechanism remains alive (it continues being operative between moderately large grains with $\lambda =$ 20–500 nm at deposition temperatures as low as $0.28T_{melting}$). Unlike the typical OR, where the exchange is driven by grain-size and/or environment difference, the exchange for the slope-selection mechanism is ruled by the kinetic stabilization of certain crystalline facets on the grain faces (i.e. by kinetic faceting). This difference in the driving forces (in which underlies the atypical nature of the operation conditions) has the following implications: (a) a grain with surface slopes lower than the selected slope cannot reach an equilibrium state with the surrounding flat surface independently of the adatom density on it because, rather than an equilibrium adatom density (like in the typical OR), in this case, there is an equilibrium grain shape for which the downhill current becomes high enough to compensate the surface adatom depletion produced by the uphill current. (b) In the absence of surrounding flat surface for compact arrangement of grains, the exchange is driven by the slope differences between neighboring grains. (c) In the case of that the slopes of the neighboring grains are far below the selected one, the exchange driven by slope difference can be interpreted straightforwardly in terms of exchange driven by grain size and/or environment difference from the grain-size dependence of the depletion range. It means that for early growth stages, the coarsening behavior produced by the slope-selection mechanism would be similar to that generated by a typical OR. On the basis of these arguments, we refer to the slope-selection mechanism as a late slope-selection driven OR. Although they have been investigated in an independent manner so far, the results presented here allow us to conclude that both the OR and slope-selection mechanisms belong to the same universal class of processes.

At this point, it deserves to be mentioned that this mechanism is responsible for the nanostructuring of the film into arrangements of pyramidal/conical single-crystalline grains, which has been correlated recently to the enhanced lasing activity of nanostructured ZnO.[41,42] The pyramidal/conical single-crystalline grains would play a double role in this effect: they act like a gain medium (since the large binding energy, ≈60 meV, of ZnO exciton) as well as a resonant Fabry–Perot cavity (since the shapes and grain coupling[42]) to produce excitonic UV laser emission at room temperature.

V. CONCLUSIONS

In this paper, we report experimental findings concerning the grain coarsening on the surface of PLD-grown ZnO[0001] films and interpret them through a comprehensive mesoscopic model of slope selection. From the evolution of the shapes and morphological environments of the grains studied by AFM, which was successfully compared with morphological features of surfaces simulated numerically; a late slope-selection-driven OR mechanism operating under atypical conditions is identified and their main characteristics addressed.

ACKNOWLEDGMENTS

Work supported by the projects 200960I182 (CSIC) and CCG10-UAM/MAT-5537 (DGUI-Comunidad de Madrid and Universidad Autónoma de Madrid). A.G.G. acknowledges the financial support of the MICINN Spanish Ministry under the project ESP2006-14282-C02-02 and PEI201160E053. Author thanks to L. Vázquez for his assistance in the AFM measurements.

*Corresponding author: agonzo@icmm.csic.es

[1]The terminology "coarsening" as used here denotes the process in which the in-plane size of the surface entities increases, without referring to the specific mechanisms (e.g. by grain growth, coalescence) that give rise to such an increase. More details in D. E. Jesson, T. P. Munt, V. A. Shchukin, and D. Bimberg, Phys. Rev. B **69**, 041302(R) (2004).

[2]G. Prévot, Phys. Rev. B **84**, 045434 (2011).

[3]V. M. Kaganer, W. Braun, and K. K. Sabelfeld, Phys. Rev. B **76**, 075415 (2007).

[4]J. G. McLean, B. Krishnamachari, D. R. Peale, E. Chason, J. P. Sethna and B. H. Cooper, Phys. Rev. B **55**, 1811 (1997).

[5]S. Kodambaka, V. Petrova, S. V. Khare, D. Gall, A. Rockett, I. Petrov, and J. E. Greene, Phys. Rev. Lett. **89**, 176102 (2002).

[6]G. Rosenfeld, K. Morgenstern, M. Esser and G. Comsa, Appl. Phys. A **69**, 489 (1999).

[7]Ostwald ripening can be realized as a particular type of abnormal (or discontinuous) grain growth between exchanging isolated entities, which are in equilibrium with local adatom density of the surface, such that the coarsening (shrinkage) of the larger (smaller) entity neither involves formation nor migration of grain boundaries. Thus, this mechanism prevails for systems with high surface-to-bulk ratios (e.g. ultra-thin films, highly rough surfaces, and nanostructured systems) in which the surface diffusion (usually higher than grain-boundary diffusion) plays a key role in the atomic exchange. Note, that in the fields of metallurgy, mineralogy, and in reference to ceramics (i.e. bulky systems), the standard grain growth implies the movement of grain boundaries.

[8]S. Aggarwal, A. P. Monga, S. R. Perusse, R. Ramesh, V. Ballarotto, E. D. Williams, B. R. Chalamala, Y. Wei, and R. H. Reuss, Science **287**, 2235 (2007).

[9]E. Vasco, C. Polop, and J. L. Sacedón, Phys. Rev. E **80**, 041604 (2009).

[10]Since the dissociation rate depends strongly on the local environment, series of partial dissociations are more probable than full dissociations, e.g. the full dissociation of a trimer into three monomers without involving the formation of an intermediate dimer is a rare event. See also Refs. 6 and 9.

[11]C. R. Stoldt, A. M. Cadilhe, C. J. Jenks, J. M. Wen, J. W. Evans, and P. A. Thiel, Phys. Rev. Lett. **81**, 2950 (1998).

[12]J. W. Evans, P. A. Thiel, and M. C. Bartelt, Surf. Sci. Rep. **61**, 1 (2006).

[13]M. Z. Allmang, L. C. Feldman and M. H. Grabow, Surf. Sci. Rep. **16**, 377 (1992).

[14]I. Horcas, R. Fernández, J. M. Gómez-Rodríguez, J. Colchero, J. Gómez-Herrero and A. M. Baró, Rev. Sci. Instrum. **78**, 013705 (2007). The equipment used in this work is an AFM Cervantes Full Mode developed by Nanotec Electronica (www.nanotec.es).

[15]E. Vasco, J. Rubio-Zuazo, L. Vázquez, C. Prieto and C. Zaldo, J. Vac. Sci. Technol. B **19**, 224 (2001).

[16]E. Vasco, C. Zaldo, and L. Vázquez, J. Phys.: Condens. Matter **13**, L663 (2001).

[17]S. C. Han, J. K. Kim, J. Y. Kim, K. K. Kim, H. Tampo, S. Niki, and J. M. Lee, J. Electrochem. Soc. **157**, D60 (2010).

[18]J. Xiao, Y. Wu, X. Bai, W. Zhang, and L. Yu, J. Phys. D: Appl. Phys. **41**, 135409 (2008).

[19]Q. J. Wang, C. Pflügl, W. F. Andress, D. Ham, M. Yamanishi, and F. Capasso, J. Vac. Sci. Technol. B **26**, 1848 (2008).

[20]A. González-González, J. L. Sacedón, C. Polop, E. Rodríguez-Cañas, J. A. Aznárez, and E. Vasco, J. Vac. Sci. Technol. A **27**, 1012 (2009).

[21]A. González-González, M. Alonso, E. Navarro, J. L. Sacedón, and A. Ruiz, Nanoscale Res. Lett. **5**, 1882 (2010).

[22]The fractal dimension is estimated as a function of the perimeter-to-grain area ratio by means of the relation: $\zeta = \frac{n-p}{n-2\sqrt{n\pi}} \log_p^{2\sqrt{n\pi}} + 1$ (see Ref. 25), in which the grain area and perimeter correspond to $A(l) \underset{l\to 0}{\to} n$ and $P(l) \underset{l\to 0}{\to} p$, respectively. Here, $A(l)$ $[P(l)]$ denotes the number of partially or fully filled [partially filled only] elements of the embedded cubic lattice (of parameter l) employed to cover the grain. The above relation was built to fulfill the following conditions: for an n-sized grain, ζ drops with increasing p at a rate $\propto 1/\ln(p)$ from $\zeta = 2$ for $p \to 2\sqrt{n\pi}$ (the shortest perimeter of a compact grain) down to $\zeta \to 1$ for $p \to n$ (the longest perimeter of a fractal grain).

[23]V. Borovikov and J. G. Amar, Phys. Rev. B **72**, 085460 (2005), and references therein.

[24]In order to compute the distribution of surface slopes and the feature contours, the 512 × 512-pixel AFM images were interpolated using Newton polynomials of order $k = 3$ so as both first and second derivatives are defined everywhere. These interpolation polynomials correlated to each other k^2 pixels of the raw images, $(512/k)^2$ being the number of areas that remain uncorrelated.

[25]A. L. Barabási and H. E. Stanley, *Fractal Concepts in Surface Growth* (Cambridge University Press, Cambridge, 1995).

[26]M. D. Johnson, C. Orme, A W. Hunt, D. Graff, J. Sudijono, L. M. Sander, and B. G. Orr, Phys. Rev. Lett. **72**, 116 (1994).

[27]B. Chakrabarti and C. Dasgupta, Phys. Rev. E **69**, 011601 (2004); **71**, 020601(R) (2005).

[28]W. Kanjanaput, S. Limkumnerd, and P. Chatraphorn, Phys. Rev. E **82**, 041607 (2010).

[29]T. S. Lo and R. V. Kohn, Physica D **161**, 237 (2002).

[30]M. D. Korzec and P. L. Evans, Physica D **239**, 465 (2010).

[31]W. L. Chan and E. Chason, J. Appl. Phys. **101**, 121301 (2007).

[32]R. Cuerno and A. L. Barabási, Phys. Rev. Lett. **74**, 4746 (1995).

[33]S. F. Edwards and D. R. Wilkinson, Proc. R. Soc. London A **381**, 17 (1982).

[34]The $\alpha/\kappa = 0.07$ ratio used in this work is in concordance with that obtained from the extrapolation of the nonlinear terms of the mesoscopic selected-slope approach described in Ref. 26 for the case $m_s = 0.41$.

[35]B. J. Wuensch and H. L. Tuller, J. Phys. Chem. Solids **55**, 975 (1994).

[36]P. V. B. Lakshmi and K. Ramachandran, Bull. Mater. Sci. **34**, 371 (2011), and references therein.

[37]S. T. Tan, X. W. Sun, X. H. Zhang, S. J. Chua, B. J. Chen, and C. C. Teo, J. Appl. Phys. **100**, 033502 (2006), and references therein.

[38]A. Janotti and C. G. Van de Walle, Phys. Rev. B **76**, 165202 (2007).

[39]A feasible comparison of the simulations with the experiments is possible only for small AFM-imaged regions, in which the random contribution [third term in Eq. (1)—that is hard to reproduce by simulation given its nature] to the surface statistics is negligible. See also Refs. 26–28.

[40]J. A. Thornton, J. Vac. Sci. Technol. **11**, 666 (1974).

[41]D. M. Bagnall, Y. F. Chen, Z. Zhu, T. Yao, S. Koyama, M. Y. Shen, and T. Goto, Appl. Phys. Lett. **70**, 2230 (1997).

[42]Z. K. Tang, G. K. L. Wong, P. Yu, M. Kawasaki, A. Ohtomo, H. Koinuma and Y. Segawa, Appl. Phys. Lett. **72**, 3271 (1998).